Contents lists available at ScienceDirect

Chemical Engineering Journal

journal homepage: www.elsevier.com/locate/cej

# Theory-guided doping of $LaCoO_3$ nanoparticles for enhanced antimicrobial performance

Junli Liu [a,*], Kaitao Zhang [a], Rongrong Shang [a], Hua Zhang [a], Jiahao Shen [a], Hui Liu [a], John Tressel [b], Yan Bao [c], Aiping Hui [d], Haijiao Xie [e], Shaowei Chen [b,*]

[a] *School of Materials Science and Engineering, Shaanxi Key Laboratory of Green Preparation and Functionalization for Inorganic Materials, Shaanxi University of Science & Technology, Xi'an, Shaanxi 710021, PR China*
[b] *Department of Chemistry and Biochemistry, University of California, Santa Cruz, CA 96064, United States*
[c] *College of Bioresources Chemical and Materials Engineering, Shaanxi University of Science and Technology, Xi'an, Shaanxi 710021, PR China*
[d] *Key Laboratory of Clay Mineral Applied Research of Gansu Province, Center of Eco-Materials and Green Chemistry, Lanzhou Institute of Chemical Physics, Chinese Academy of Sciences, Lanzhou 730000, PR China*
[e] *Hangzhou Yanqu Information Technology Co., Ltd, Y2, 2nd Floor, Building 2, Xixi Legu Creative Pioneering Park, 712 Wen'er West Road, Xihu District, Hangzhou, Zhejiang 310003, PR China*

ARTICLE INFO

*Keywords:*
$LaCoO_3$
Cerium and aluminum doping
Oxygen vacancy
Density functional theory
Antibacterial activity

ABSTRACT

Perovskite-type lanthanum cobaltate ($LaCoO_3$) has been attracting extensive attention in photocatalysis; yet the performance is generally limited by the low structural defects and poor oxygen migration. Herein, results from first principles calculations show that Al and Ce codoping at the A and B sites of $LaCoO_3$ can induce the formation of oxygen vacancies, which, along with the exposed Co (012) facets, facilitate the adsorption of oxygen and water molecules, a critical step in the photocatalytic production of reactive oxygen species that are known as potent antimicrobial agents. Motivated by these theoretical insights, Ce and Al codoped $LaCoO_3$ is prepared experimentally via a simple sol–gel procedure. Spectroscopic measurements show that the cationic doping leads to the generation of abundant oxygen vacancies and $Ce^{4+}/Ce^{3+}$ species, fast electron transport, as well as a reduced band gap, as compared to the undoped counterpart. These unique structural characteristics enhance the separation and transport of photogenerated carriers and hence the generation of reactive oxygen species. Indeed, the obtained $La_{0.9}Ce_{0.1}Co_{0.9}Al_{0.1}O_3$ exhibits excellent photocatalytic antibacterial activity, where 98.8% of *Escherichia coli* is eliminated with $La_{0.9}Ce_{0.1}Co_{0.9}Al_{0.1}O_3$ at 1 mg $mL^{-1}$ under visible photoirradiation for 30 min, in comparison to only 46.8% with undoped $LaCoO_3$. These results underline the significance of structural engineering in enhancing the photocatalytic activity of perovskite materials for antibacterial applications.

## 1. Introduction

Bacterial infections have become one of the most serious threats to public health, which may arise in postoperative wounds, bacterial spoilage in food breeding, and illnesses caused by the misuse of antibiotics [1]. Studies have shown that more than half of bacterial infections are caused by Gram-negative *Escherichia coli* (*E. coli*) and Gram-positive *Staphylococcus aureus* (*S. aureus*) [2]. Moreover, the misuse/abuse of antibiotics has led to an increase in bacterial resistance, resulting in the emergence and rapid spread of "superbugs" that pose a great danger to the ecological environment and human health [3]. Thus, rational design and engineering of high-performance, low-cost antibacterial agents have been attracting extensive interest. It has been shown that chemically synthesized nanoparticles (NPs) may possess unique antibacterial activity towards both Gram-positive and Gram-negative bacteria [4–6]. For example, silver nanoparticles mixed with titanium dioxide nanopowders can inhibit bacterial growth [7,8], and gold, copper, and silver nanoparticles have been exploited for water disinfection [9].

Recently, photocatalysis has emerged as a green technology to combat bacterial infection [10], where the development of effective, stable, and low-cost semiconductor photocatalysts plays a key role, such as metal oxides [11], metal sulphides [12], metal polyhalides [13–15], polymeric carbon nitride [16], and perovskite ($ABO_3$) [17], due to the production of a range of radical species [18,19]. Among these, perovskite-type lanthanum cobaltate ($LaCoO_3$) has been attracting particular attention [20]. However, the relatively wide forbidden

---

* Corresponding authors.
*E-mail addresses:* liujunli042@163.com (J. Liu), shaowei@ucsc.edu (S. Chen).

https://doi.org/10.1016/j.cej.2023.142710
Received 3 February 2023; Received in revised form 19 March 2023; Accepted 29 March 2023
Available online 1 April 2023

**Fig. 1.** Schematic diagram of sample preparation by the sol–gel method.

bandgap of $LaCoO_3$ greatly limits its solar energy harvesting efficiency and hence the photocatalytic activity due to a high recombination rate of photogenerated electron-hole pairs [21]. Such issues can be mitigated by deliberate structural engineering so that the electronic energy structure can be manipulated, in particular, for enhanced absorption in the visible light range.

Notably, the $BO_6$ octahedral structure of $Co^{3+}$ and $O^{2-}$ and the $e_g$ orbitals have been known to determine the adsorption energetics of reactant species onto $LaCoO_3$ [17,22]. The Co 3d orbitals act as the conduction band (CB) of $LaCoO_3$, and modulate the upward shift of the O 2p orbitals (valence band, VB) relative to the Fermi level. This facilitates the formation of oxygen defects in the crystal structure [22], and enhances the conduction of oxygen ions and the catalytic activity of the perovskite. Therefore, one can see that the electronic properties of $LaCoO_3$ can be readily manipulated by the introduction of cationic dopants into the lattice, as the replacement of $La^{3+}$ and/or $Co^{3+}$ by foreign cations is anticipated to induce the formation of oxygen vacancies and accelerate the migration of oxygen species, such as surface adsorbed oxygen and lattice oxygen [23,24]. For instance, the introduction of Ce in the variable oxidation state ($Ce^{4+}/Ce^{3+}$) at the A sites can increase the surface area, reduce the grain size, and produce a high number of defects, leading to an increase of both oxygen storage and oxygen conversion active species and hence enhanced optical absorption and oxidation/reduction activity of $LaCoO_3$ [25,26]. Wang et al. [27] showed that the methane reforming activity of $La_{0.4}Ce_{0.6}Ni_{0.5}Fe_{0.5}O_3$ was enhanced due to the formation of low-valence $Ni^{2+}$ and abundant oxygen vacancies induced by $Ce^{4+}$ at the A sites. Tang et al. [28] used $K^+$ to partially replace $La^{3+}$ at the A sites to promote the formation of $Co^{4+}$, achieving a high oxidation activity due to the formation of abundant oxygen vacancies.

In general, the B site of $LaCoO_3$ consists of transition metal elements to modulate its electronic structure and oxygen vacancy concentration for high catalytic performance. For instance, Lu et al. [29] found that the photocatalytic activity of $LaCoO_3$ towards phenol degradation could be markedly enhanced by introducing transition metal elements, such as Mn, Fe, and Cu, at the B sites, among which $LaCo_{0.4}Cu_{0.6}O_3$ stood out with the best performance. Al-doped $LaCoO_3$ has also been prepared for photocatalysis. For instance, doping of aliovalent metal cations to $SrTiO_3$ was found to lead to an apparent quantum yield (AQY) of 56% at 360 nm and an effective water splitting efficiency of 0.4% under simulated sunlight [30,31]. This was accounted for by the Al dopants at the B sites that inhibited the recombination of electron-hole pairs [32]. In fact, for $Al^{3+}$-modified materials, mid-infrared transient absorption spectroscopy measurements confirmed an extended electron-hole carrier lifetime [33]. In these studies, the adsorption capacity and oxygen migration efficiency of the catalysts can be readily altered by adjusting the valence and species of the A and B sites. Nevertheless, thus far the photocatalytic activity of $LaCoO_3$ has mostly focused on the degradation of organic pollutants [25,29,34], whereas few studies have been reported in antibacterial applications.

In the present study, Ce and Al-codoped $LaCoO_3$ is prepared via a facile sol–gel method, where the doping of Ce and Al into the A and B sites of the $LaCoO_3$ lattice leads to the modulation of surface Co ions and the formation of oxygen vacancies, and hence a remarkable photocatalytic antibacterial performance towards both Gram-negative and Gram-positive bacteria. This experimental design is motivated by results from computational studies based on density functional theory (DFT) calculations, where the non-active center atoms, in particular, oxygen vacancies, are found to improve the photoresponse, reduce the material bandgap, and facilitate photocarrier separation. Among the series, the

$La_{0.9}Ce_{0.1}Co_{0.9}Al_{0.1}O_3$ sample exhibits the best antibacterial performance, due to excellent adsorption and charge transfer properties. Results from this work highlights the unique potential of $LaCoO_3$-based materials as high-performance antimicrobial agents.

## 2. Experimental section

### 2.1. Chemicals

Lanthanum nitrate hexahydrate ($La(NO_3)_3{\cdot}6H_2O$, $\geq$99%), cerium nitrate hexahydrate ($Ce(NO_3)_3{\cdot}6H_2O$, $\geq$98%), aluminum nitrate nonahydrate ($Al(NO_3)_3{\cdot}9H_2O$, $\geq$98%), and cobalt nitrate hexahydrate ($Co(NO_3)_2{\cdot}6H_2O$, $\geq$98%) were purchased from Macklin Biochemicals Co., Ltd. Sodium hydroxide (NaOH, $\geq$96%), ammonia solution ($NH_3{\cdot}H_2O$ 25%), and sodium sulfate anhydrous ($Na_2SO_4$, $\geq$99%) was purchased from Tianjin Tianli Chemical Reagents Co., Ltd. All chemical reagents were of analytical reagent grade.

### 2.2. Sample preparation

A series of $La_{1-x}Ce_xCo_{1-y}Al_yO_3$ samples ($0 < x, y < 1$) were synthesized by the sol–gel method, where the A and B sites were respectively doped with Ce and Al at systematically varied concentrations. Experimentally, lanthanum nitrate hexahydrate ($La(NO_3)_3{\cdot}6H_2O$), cerium nitrate hexahydrate ($Ce(NO_3)_3{\cdot}6H_2O$), aluminum nitrate nonahydrate ($Al(NO_3)_3{\cdot}9H_2O$), cobalt nitrate hexahydrate ($Co(NO_3)_2{\cdot}6H_2O$) and citric acid ($C_6H_8O_7$) were dissolved in deionized water at a molar ratio of 1:1.2 of total metal ions to citric acid but with varied initial feeds, and the solution pH was adjusted to 9 by ammonia ($NH_3{\cdot}H_2O$). The solution was placed in an 85 °C water bath until a wet gel was formed. The gel was dried and calcined at 600 °C in air to obtain the corresponding perovskite nanoparticles, as illustrate in Fig. 1.

### 2.3. Characterization

The crystal structure of the perovskite samples was determined by X-ray diffraction (XRD) measurements using a Rigaku D/Max-2200 diffractometer (Cu $K_\alpha$, $\lambda = 0.154$ nm) at a scanning step of 0.02° within the range of 20 to 80°. The morphology of the samples was examined with a scanning electron microscope (SEM, S4800) and transmission electron microscope (TEM, Tecnai G2 F20-Twin), and elemental analysis was performed with an attached energy-dispersive X-ray spectrometer (EDS). The optical absorption was tested with a Lambda-950 UV–vis spectrophotometer within the range of 200 to 800 nm. The valence states were characterized by X-ray photoelectron spectroscopy (XPS, AXIS SUPRA) measurements with the C 1 s binding energy (284.6 eV) as the calibration reference. Infrared spectra were acquired with a Bruker VERTEX 80v instrument. The recombination efficiency of the photogenerated electron-hole pairs was characterized by transient photocurrent measurements with an Ag/AgCl reference electrode in 0.1 M $Na_2SO_4$. Photoluminescence (PL) spectroscopy measurements were carried out with an F-7000 spectrometer at the excitation wavelength of 420 nm with an excitation/emission slit of 5.0 nm. Electron paramagnetic resonance (EPR) measurements were conducted with a JEOL-JES-FA200 instrument and 5,5-dimethyl-1-pyrroline (DMPO) as the spin-trapping agent.

### 2.4. Photodynamic antibacterial activity

The bacteria solution in logarithmic growth phase and the samples prepared above were mixed at a volume ratio of 1:1, and the mixture was placed under visible light for 0, 10, 20 and 30 min (100 mW $cm^{-2}$, Shenzhen Jiansheng Lighting Co., Ltd.) after adsorption equilibrium in the dark. 28 μL of the above solution was evenly applied on the surface of a solid agar medium and incubated at 37 ℃ for 20 h, where the number of surviving bacterial colonies was counted by ImageJ® software.

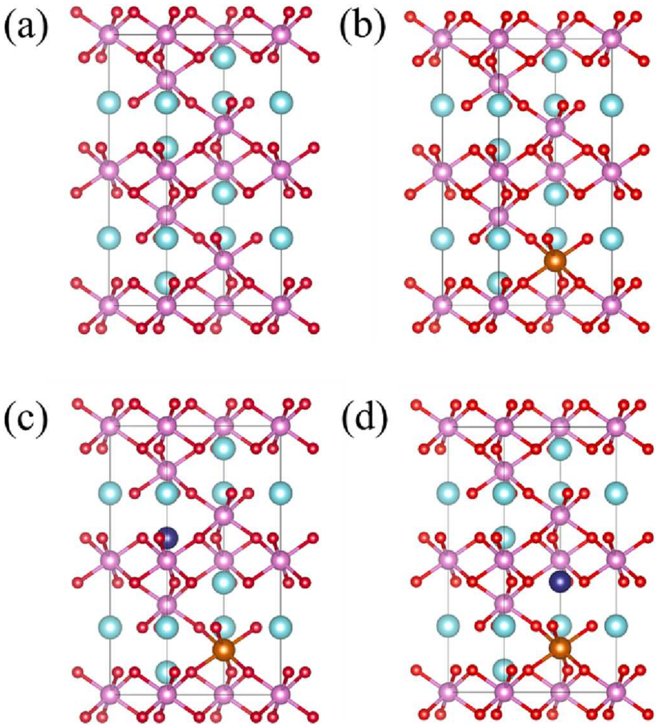

**Fig. 2.** Crystal structures of (a) $LaCoO_3$, (b) $LaCo_{0.9}Al_{0.1}O_3$, and (c,d) $La_{0.9}Ce_{0.1}Co_{0.9}Al_{0.1}O_3$ after optimization. Color legends: O, red; Co, pink; La, cyan; and Ce, dark blue. The coordination numbers of the surface species are highlighted in each structure.

### 2.5. SEM analysis

The samples were mixed with bacteria under shaking, after which the bacterial cells were centrifuged and fixed with a glutaraldehyde (2.5% mass fraction) solution at 4 ℃ for 12 h. The fixed bacteria were rinsed three times with a 0.1 M phosphate buffer solution (PBS) and dehydrated in a gradient of 30%, 50%, 70%, 80%, 90% and 100% ethanol for 10 min, before being dried in a fume hood for 1 h and in a 50 ℃ oven for 2 h.

### 2.6. Bacterial fluorescence labeling

Bacteria in logarithmic phase were inoculated in a fresh LB medium at a ratio of 1:10, into which the samples and bacteria were added at a volume ratio of 1:1. The mixture was shaken at 37 ℃ for 10 h in a constant-temperature water bath shaker, followed by centrifugation and rinsing twice to collect the bacteria. The collected bacteria were stained with propidium iodide (PI, 15 mM) for 15 min and SYTO 9 (3 mM) for 10 min in the dark, before being examined with a LSM800 laser confocal fluorescence microscope.

### 2.7. Computational study

The Vienna Ab Initio Simulation Package (VASP) [35] was adopted to perform all DFT calculations within the generalized gradient approximation (GGA) using the Perdew-Burke-Ernzerhof (PBE) formulation [36]. The projection augmented wave (PAW) [37] potentials were used to describe ionic cores, and valence electrons were considered using a plane wave basis set with a kinetic energy cutoff of 520 eV. Partial occupancies of the Kohn – Sham orbitals were allowed using the Gaussian smearing method with a width of 0.05 eV. The electronic energy was regarded as self-consistent when the energy change was

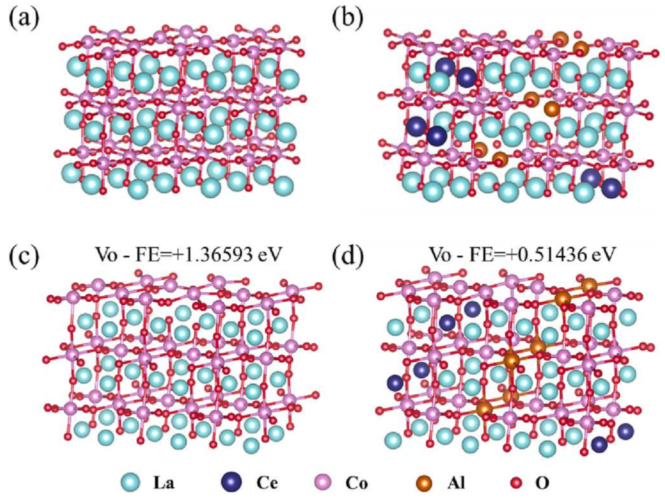

**Fig. 3.** DFT-based optimized slab structure corresponding to the unique low-index (0 1 2) facets of (a) rhombohedral $LaCoO_3$, (b) $La_{0.9}Ce_{0.1}Co_{0.9}Al_{0.1}O_3$, (c) Vo-decorated $LaCoO_3$, and (d) Vo-decorated $La_{0.9}Ce_{0.1}Co_{0.9}Al_{0.1}O_3$. Color legends: red, pink, cyan and dark blue for O, Co, La and Ce, respectively. The coordination numbers of the surface species are highlighted in each structure.

smaller than $10^{-5}$ eV. Moreover, a geometrical optimization was considered convergent when the force change was $< 0.05$ eV Å$^{-1}$. Grimme's DFT-D3 methodology [38] was used to describe the dispersion interactions. The Brillouin zone integral used the surface structures of 2 × 2 × 1 monkhorst pack K-point sampling. Finally, the adsorption energies ($E_{ads}$) were calculated as $E_{ads} = E_{ad/sub} - E_{ad} - E_{sub}$, where $E_{ad/sub}$, $E_{ad}$, and $E_{sub}$ were the total energies of the optimized adsorbate/substrate system, the adsorbate in the gas phase, and the clean substrate, respectively.

## 3. Results and discussion

### 3.1. Computational studies

The structures of Ce, Al-codoped $LaCoO_3$ were firstly optimized by computational studies. Fig. 2 shows the optimized crystal structures of (a) $LaCoO_3$, (b) $LaCo_{0.9}Al_{0.1}O_3$, and (c, d) $La_{0.9}Ce_{0.1}Co_{0.9}Al_{0.1}O_3$. The latter entails two different crystal configurations, one with Ce situated away from Al ($E_{total}$ = -221.2958 eV, Fig. 2c), and the other with Ce situated close to Al ($E_{total}$ = -221.1059 eV, Fig. 2d). Secondly, the optimization of the low-index (0 1 2) crystal plane was used as a prerequisite for the introduction of oxygen vacancy (Vo) defects. Hence, DFT-based optimized slab structures were obtained corresponding to the unique low-index (0 1 2) rhombohedral $LaCoO_3$ and $La_{0.9}Ce_{0.1}Co_{0.9}Al_{0.1}O_3$ facets (Fig. 3a-b). To investigate the effect of doping on oxygen vacancy formation in depth, DFT calculations were carried out to compare the oxygen vacancy formation energy on the surface of $LaCoO_3$ and $La_{0.9}Ce_{0.1}Co_{0.9}Al_{0.1}O_3$, which was lower on the latter (Vo – FE = +0.51436 eV, Fig. 3d) than on the former (Vo – FE = +1.36593 eV, Fig. 3c). This is because oxygen vacancies can produce defective-state energy levels, function as electron traps for carrier separation, and act as active centers for catalytic processes [39]. Taken together, these results show that codoping at the A and B sites can induce the formation of defect states in a way that contributes to the formation of oxygen vacancies.

To examine the effects of oxygen vacancies on the production of reactive oxygen species (ROS) for antibacterial applications, DFT calculations were carried out to compare the adsorption of $H_2O$ and $O_2$ on the surfaces of Vo-decorated $LaCoO_3$ ($LaCoO_3$-Vo) (Fig. 4a1 and c1) and $La_{0.9}Ce_{0.1}Co_{0.9}Al_{0.1}O_3$ ($La_{0.9}Ce_{0.1}Co_{0.9}Al_{0.1}O_3$-Vo) (Fig. 4b1 and d1). Notably, the adsorption energies of $H_2O$ and $O_2$ increased from −1.36914 and −0.53921 eV on $LaCoO_3$-Vo to −1.78993 and −1.10859 eV on $La_{0.9}Ce_{0.1}Co_{0.9}Al_{0.1}O_3$-Vo, suggesting that oxygen vacancies drastically facilitate the adsorption of $H_2O$ and $O_2$ molecules [40], a key step in the photocatalytic generation of ROS and the eventual antibacterial pathway [41,42].

Additionally, from the charge density difference diagrams (Fig. 4a2-d2), one can see that charge transfer may occur between the crystal surface and adsorbed $H_2O$ and $O_2$ molecules. This indicates that oxygen vacancies indeed enhance chemical adsorption [43]. In particular, the adsorption of $H_2O$ and $O_2$ on $La_{0.9}Ce_{0.1}Co_{0.9}Al_{0.1}O_3$-Vo boosts charge transfer and enables the generation of ROS (e.g., •OH and $\bullet O_2^-$). In addition, the presence of $Ce^{3+}/Ce^{4+}$ (Fig. 4b2 and d2) enhances charge transfer within the crystal, not just on the sample surface, resulting in efficient catalytic performance, as observed below [44,45].

### 3.2. Characterization of $La_{0.9}Ce_{0.1}Co_{0.9}Al_{0.1}O_3$

Motivated by the computational insights, a series of $La_{1-x}Ce_xCo_{1-y}Al_yO_3$ samples were then prepared via a facile sol-gel method. The XRD

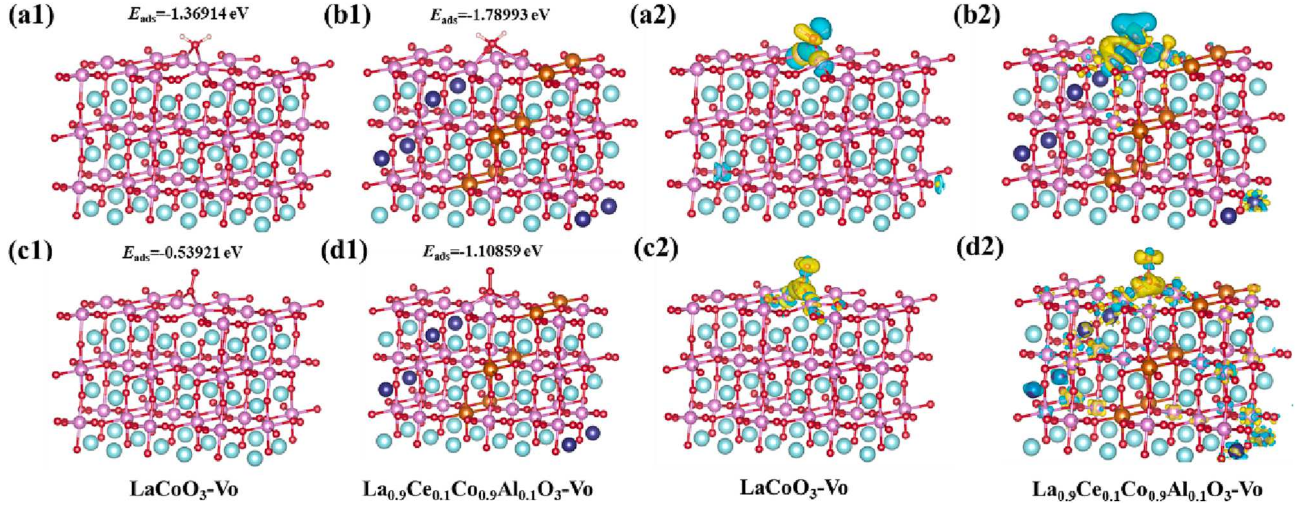

**Fig. 4.** Optimized structures of (a1, b1) $H_2O$ and (c1, d1) $O_2$ absorption on the low-index (0 1 2) facets of rhombohedral $LaCoO_3$-Vo and $La_{0.9}Ce_{0.1}Co_{0.9}Al_{0.1}O_3$-Vo. Charge density differences of optimized (a2, b2) $H_2O$ and (c2, d2) $O_2$ absorption on $LaCoO_3$-Vo and $La_{0.9}Ce_{0.1}Co_{0.9}Al_{0.1}O_3$-Vo. Color legend: red, pink, cyan and dark blue for O, Co, La and Ce, respectively. The coordination numbers of the surface species are highlighted in each structure. In panels (a2-d2), light blue represents charge loss and yellow denotes charge gain.

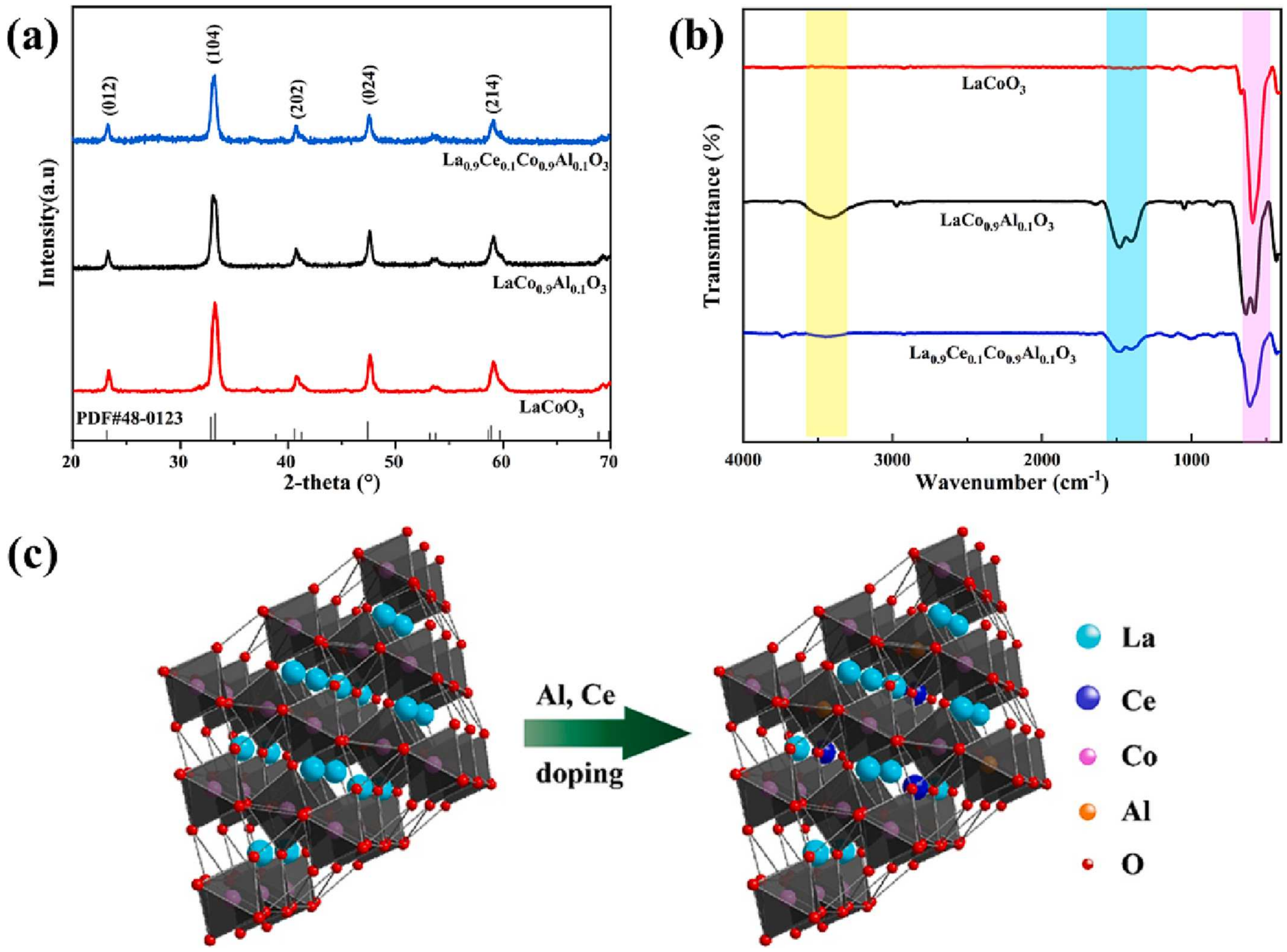

**Fig. 5.** (a) XRD patterns and (b) FTIR spectra of $La_{0.9}Ce_{0.1}Co_{0.9}Al_{0.1}O_3$. (c) Schematic diagram of Ce and Al substitution in a $LaCoO_3$ cell.

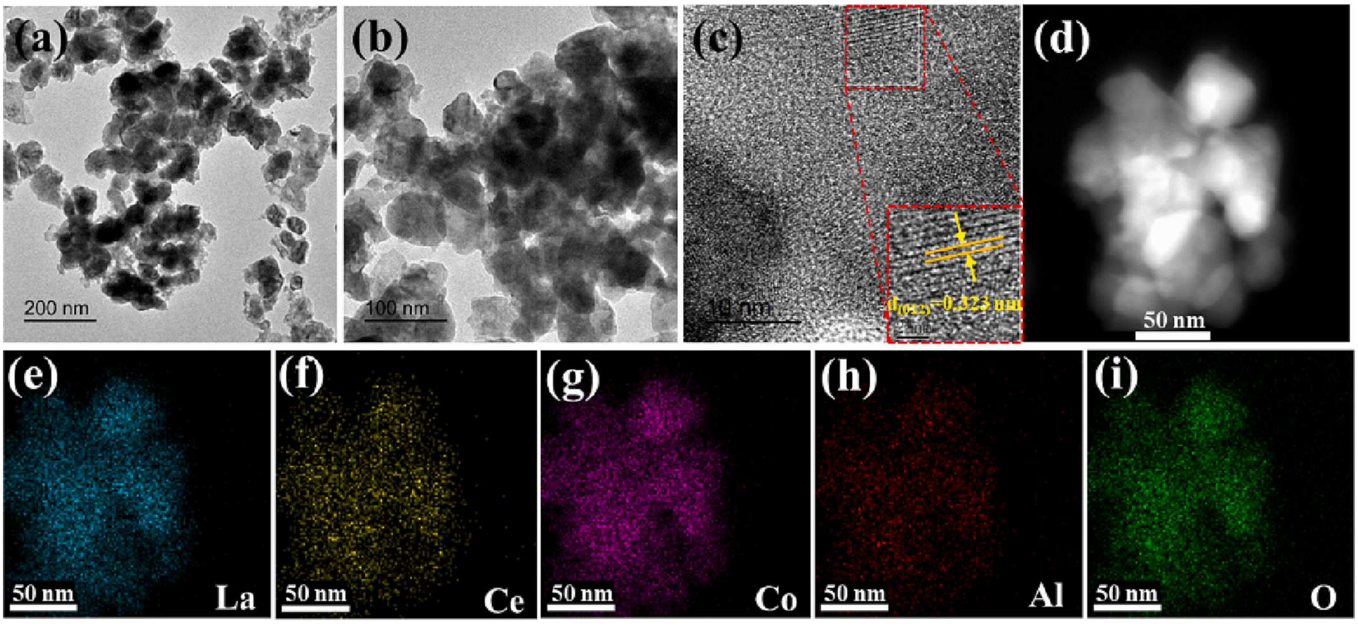

**Fig. 6.** (a, b) TEM images, (c) HRTEM image and (d-i) EDS-based elemental maps of $La_{0.9}Ce_{0.1}Co_{0.9}Al_{0.1}O_3$. Scale bars are (a) 200 nm, (b) 100 nm, (c) 10 nm, and (d-i) 50 nm.

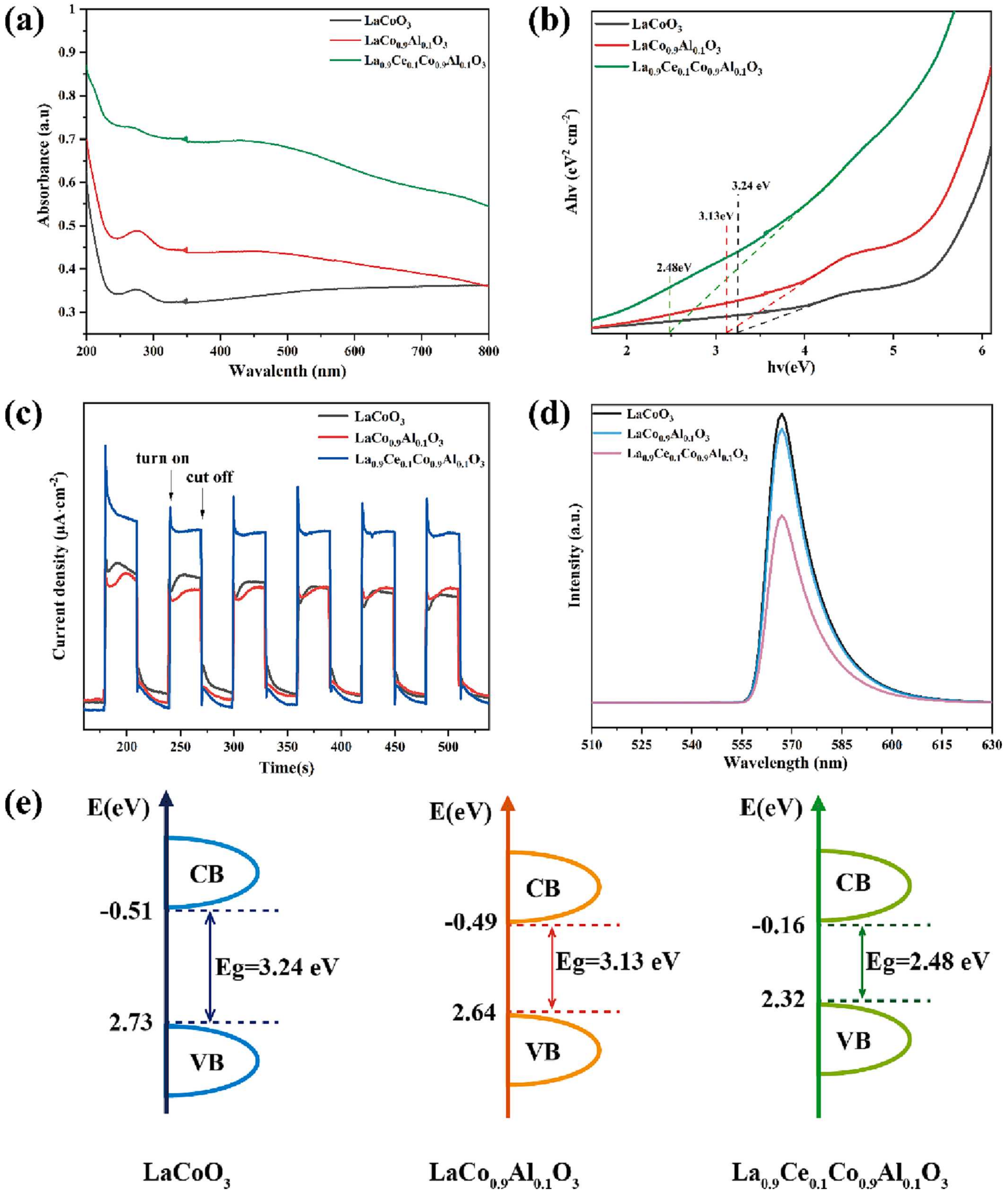

**Fig. 7.** (a) UV–vis diffuse reflectance spectra, (b) Tauc plots, (c) transient photocurrent responses, (d) PL emission spectra (excitation wavelength 325 nm), and (e) band diagrams of $LaCoO_3$, $LaCo_{0.9}Al_{0.1}O_3$, and $La_{0.9}Ce_{0.1}Co_{0.9}Al_{0.1}O_3$.

patterns of $LaCoO_3$, $LaCo_{0.9}Al_{0.1}O_3$ and $La_{0.9}Ce_{0.1}Co_{0.9}Al_{0.1}O_3$ are shown in Fig. 5a. One can see that all three samples possess the diffraction peaks at $2\theta = 23.2^\circ$, $33.2^\circ$, $40.6^\circ$, $47.5^\circ$ and $59.0^\circ$ that can be ascribed to the (012), (104), (202), (024), (214) crystal planes of rhombohedral $LaCoO_3$ (JCPDS No: 48–0123), respectively [25], suggesting almost identical crystal structure. In fact, the diffraction patterns remained virtually unchanged with the doping of Al even at $y > 0.1$ (Figure S1a), due to the consistent phase property of $LaCoO_3$ and $LaAlO_3$

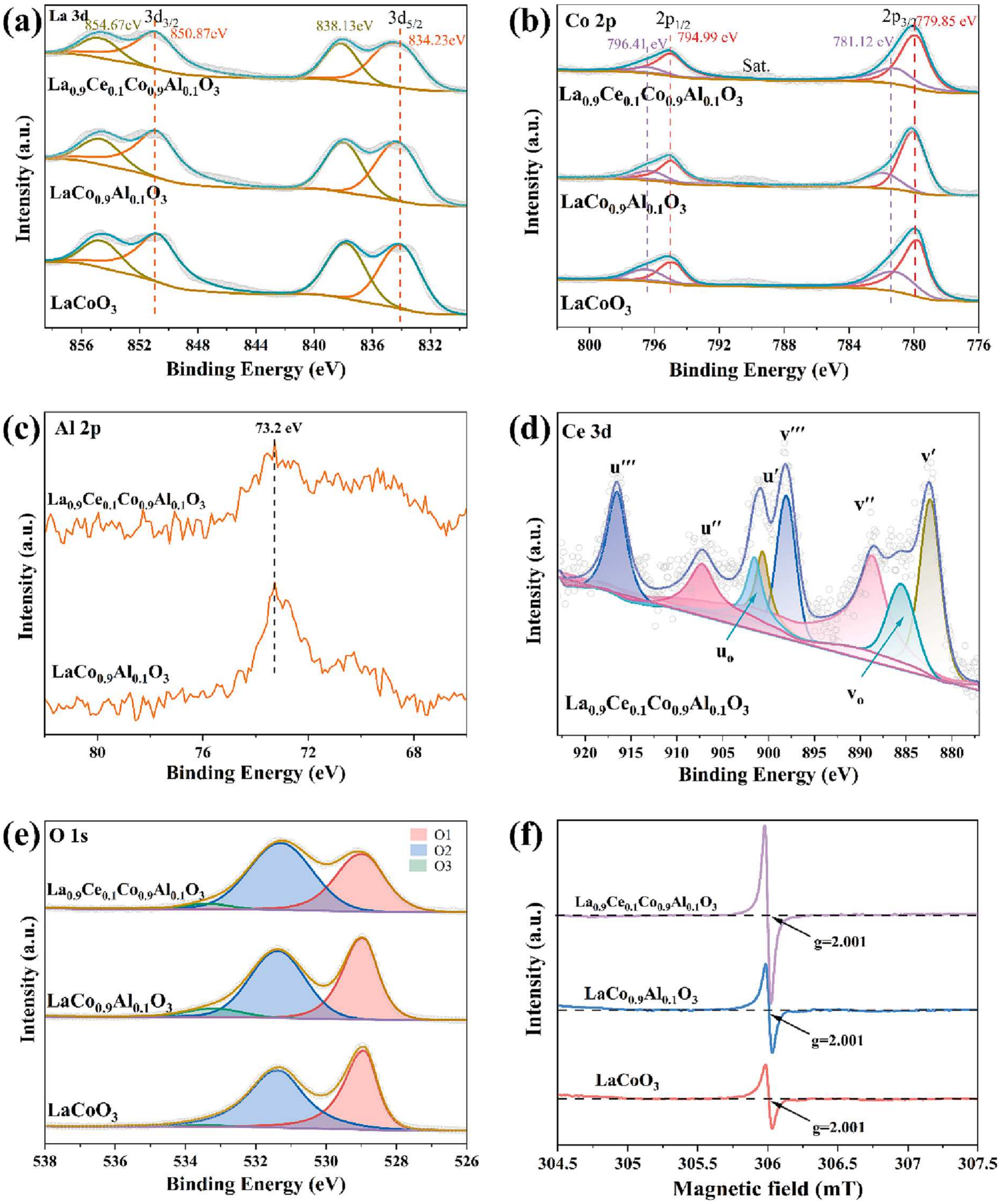

**Fig. 8.** XPS spectra of the (a) La 3d, (b) Co 2p, (c) Al 2p, (d) Ce 3d, (e) O 1s electrons of $LaCoO_3$, $LaCo_{0.9}Al_{0.1}O_3$, and $La_{0.9}Ce_{0.1}Co_{0.9}Al_{0.1}O_3$. (f) EPR spectra of $LaCoO_3$, $LaCo_{0.9}Al_{0.1}O_3$, and $La_{0.9}Ce_{0.1}Co_{0.9}Al_{0.1}O_3$.

[46]. Yet, from the zoom-in of the (1 0 4) diffraction peak in Figure S1b, it can be seen that the peak position shifts slightly to a higher angle with increasing Al content from $2\theta = 33.2^\circ$ at $y = 0$ to $2\theta = 33.3^\circ$ at $y = 0.5$, likely due to the smaller ionic radius of $Al^{3+}$ (0.53 Å) than that of $Co^{3+}$ (0.74 Å) [46]. This suggests that the samples at low doping ($x, y < 0.1$) largely retained the perovskite structure [47]. However, as $Ce^{3+}$ (1.01 Å) and $Ce^{4+}$ (0.87 Å) are smaller than $La^{3+}$ (1.03 Å) [44], lattice distortion is prone to occur, leading to the emergence of a new phase ($La_2O_3$, JCPDS No: 22–0369) [48], which appeared at $x > 0.1$ (Figure S2a). It has been previously reported [26] that the change of the structure of perovskite rhombohedral phase depends on the size of the substituent lanthanides, and lattice distortion generates oxygen vacancies. The substitution at the La lattice (A) sites leads to different orders of ions and vacancies, which impacts the eventual catalytic activity.

The crystalline grain size (D) of the $La_{0.9}Ce_{0.1}Co_{0.9}Al_{0.1}O_3$ perovskites was then evaluated by the Scherrer equation, $D = \frac{K\lambda}{\beta COS\theta}$, where λ is the X-ray wavelength (0.1540 nm), K is the constant (0.91), β is the full-width at half-maximum of the diffraction peak, and θ is the diffraction angle. From the calculation, one can see that the average grain size of the

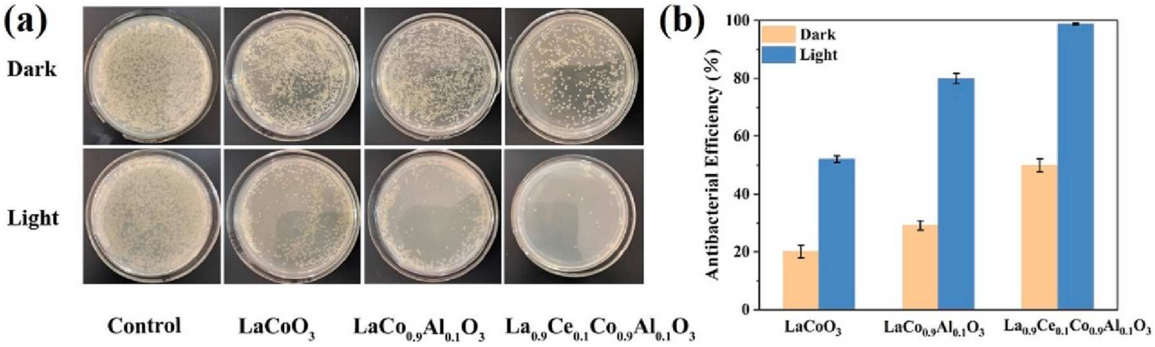

**Fig. 9.** (a) Photographs of *E. coli* growth before and after the treatment of $LaCoO_3$, $LaCo_{0.9}Al_{0.1}O_3$ and $La_{0.9}Ce_{0.1}Co_{0.9}Al_{0.1}O_3$ in the dark and under visible light irradiation for 30 min. (b) Summary of the antimicrobial efficiency.

$La_{0.9}Ce_{0.1}Co_{0.9}Al_{0.1}O_3$ was within the range of 20 to 30 nm.

In FTIR measurements (Fig. 5b), all samples can be seen to show vibrational bands at *ca.* 3450, 1480 and 1360 $cm^{-1}$, due to the O-H stretching, bending and shear vibrations of adsorbed $H_2O$ molecules, respectively [48]. The peak at 600 and 660 $cm^{-1}$ correspond to the Co-O bending vibration and Al-O stretching vibration of $LaCo_{0.9}Al_{0.1}O_3$, respectively [21,49]. In addition, the vibrational bands below 700 $cm^{-1}$ changed significantly with the Ce doping (Fig. 5c and S2b). Figure S1c depicts the corresponding UV–vis diffuse reflectance spectra. As compared to undoped $LaCoO_3$, one can see that the overall absorption was enhanced with Al doping across the wide wavelength range of 200 to 800 nm, with the absorption edge extended to the visible range from the UV region.

The morphology and elemental distribution of the $La_{0.9}Ce_{0.1}Co_{0.9}Al_{0.1}O_3$ sample were then analyzed by TEM measurements. From Fig. 6a-b, the sample can be seen to consist of a number of nanoparticles of 50–100 nm in diameter. High-resolution TEM measurements of the nanoparticles (Fig. 6c) show clearly-defined lattice fringes with an interplanar spacing of 0.323 nm that can be ascribed to the (0 1 2) planes of $LaCoO_3$ (JCPDS No: 48–0123). In EDS-based elemental mapping analysis (Fig. 6d-i), the elements of La (cyan), Ce (yellow), Co (purple), Al (red), O (green) can be found to be evenly distributed across the entire sample, consistent with the above XRD results.

The UV–vis diffuse reflectance spectra of $LaCoO_3$, $LaCo_{0.9}Al_{0.1}O_3$ and $La_{0.9}Ce_{0.1}Co_{0.9}Al_{0.1}O_3$ are shown in Fig. 7a. One can see that the absorption range extends from the UV to visible region upon Ce doping, and $La_{0.9}Ce_{0.1}Co_{0.9}Al_{0.1}O_3$ exhibited the highest absorbance. This is likely due to partial substitution of La by Ce at the A sites that created lattice defects and enhanced the transfer of electrons from the O 2p orbital [26]. When the doping amount ($x$) of Ce was $> 0.1$ (Figure S3a), the absorption intensity started to decrease, likely due to the destruction of the crystal structure of the sample. Fig. 7b and S3b shows the corresponding Tauc plots, from which the band gaps of $LaCoO_3$ and $La_{1-x}Ce_xCo_{0.9}Al_{0.1}O_3$ were estimated to be 3.13, 2.79, 2.48, 3.05, and 2.71 eV at $x = 0$, 0.05, 0.1, 0.15, and 0.2, respectively, in comparison to 3.24 eV for pristine $LaCoO_3$. That is, the utilization of visible light was maximized by the doping of Ce at $x = 0.1$ (and Al at $y = 0.1$, Figure S3) in $LaCoO_3$, which would be beneficial to improve the photocatalytic antibacterial performance (vide infra).

This is consistent with the photocurrent profiles of the $LaCoO_3$, $LaCo_{0.9}Al_{0.1}O_3$ and $La_{0.9}Ce_{0.1}Co_{0.9}Al_{0.1}O_3$ samples, as shown in Fig. 7c. Both $LaCo_{0.9}Al_{0.1}O_3$ and $La_{0.9}Ce_{0.1}Co_{0.9}Al_{0.1}O_3$, with partial cationic substitutions, can be seen to exhibit stable photocurrent intensities under visible light irradiation, whereas the photocurrents of undoped $LaCoO_3$ decayed gradually with increasing irradiation time, due to recombination of photogenerated electrons and holes [45]. Notably, it can be seen that $La_{0.9}Ce_{0.1}Co_{0.9}Al_{0.1}O_3$ exhibited the largest photocurrents, suggesting a highest separation efficiency of the photogenerated electron-hole pairs. This is further confirmed in PL emission measurements (Fig. 7d), where the $LaCoO_3$, $LaCo_{0.9}Al_{0.1}O_3$, and $La_{0.9}Ce_{0.1}Co_{0.9}Al_{0.1}O_3$ samples can all be seen to exhibit a PL emission peak at 570 nm. Compared to the undoped $LaCoO_3$, the emission of the Ce and Al codoped samples was significantly quenched, consistent with enhanced separation of the photogenerated electron-hole pairs [45,50].

In addition, the CB and VB energies of the samples can be determined by the following equations [51],

$$E_{CB} = \chi - E^e - 0.5E_g \tag{1}$$

$$E_{VB} = E_{CB} + E_g \tag{2}$$

where $E_g$ is the bandgap energy of the sample, $E^e$ is the energy of free electrons vs. hydrogen (4.5 eV), and $\chi$ is the electronegativity of the material. Based on the bandgap of the materials, the $E_{CB}$ and $E_{VB}$ were estimated and listed in Table S1 for $LaCoO_3$, $LaCo_{0.9}Al_{0.1}O_3$ and $La_{0.9}Ce_{0.1}Co_{0.9}Al_{0.1}O_3$, and graphically presented in Fig. 7e.

The valence states of lanthanum, cobalt, aluminum, cerium, and oxygen in the $LaCoO_3$, $LaCo_{0.9}Al_{0.1}O_3$, and $La_{0.9}Ce_{0.1}Co_{0.9}Al_{0.1}O_3$ samples were then characterized by XPS measurements. From the survey spectra in Figure S4, the Al 2p, O 1 s, Co 2p, La 3d and Ce 3d electrons can be clearly identified at 73, 530, 780, 836, and 882 eV, respectively. On the basis of the integrated peak areas, the elemental composition was estimated to be 14.21 at% for La, 15.67 at% for Co, and 70.12 at% for O for the undoped $LaCoO_3$ (Table S2), which is rather close to the stoichiometric ratio. For the doped samples, the elemental contents were also consistent with the initial feeds, 13.67 at% for La, 1.44 at% for Ce, 11.44 at% for Co, 1.23 at% for Al, and 72.22 at% for O in $La_{0.9}Ce_{0.1}Co_{0.9}Al_{0.1}O_3$, in comparison to 14.79 at% for La, 11.91 at% for Co, 1.36 at% for Al, and 71.94 at% for O in $LaCo_{0.9}Al_{0.1}O_3$ (Table S2).

The high-resolution La 3d scans are shown in Fig. 8a, where the doublet at 850.87/834.23 eV can be assigned to the $3d_{3/2}/3d_{5/2}$ electrons of $La^{3+}$ [26,47]. Two additional peaks can be resolved at 854.67 and 838.13 eV, due to electron migration from the O 2p orbitals to the empty La 4f orbitals [21]. In the high-resolution profiles of the Co 2p electrons (Fig. 8b), two doublets can be resolved at 794.99/779.85 eV and 796.41/781.24 eV that can be assigned to the $2p_{3/2}/2p_{1/2}$ electrons of $Co^{3+}$ and $Co^{2+}$, respectively [34,47,52].

Notably, whereas Al is doped into the sample in the form of $Al^{3+}$, the Al 2p binding energy (ca. 73.2 eV) was markedly lower than that of standard $Al^{3+}$ (74.7 eV) [53] (Fig. 8c). This is likely because of the formation of Co-O-Al bonds where the electron density of O was biased toward Al due to the stronger electronegativity of Al than Co [45,54]. The high-resolution scan of the Ce 3d electrons is depicted in Fig. 8d, which confirms that the Ce atoms were successfully doped into the sample in the forms of $Ce^{3+}$ and $Ce^{4+}$ [55] (Table S3). Three oxygen species were deconvoluted in the high-resolution O 1 s spectra (Fig. 8e), where the peaks at 528.9 eV (O1), 531.4 eV (O2) and 533.2 eV (O3) correspond to lattice oxygen, oxygen vacancies, and surface adsorbed oxygen, respectively [56]. It is worth noting that the ratio of the

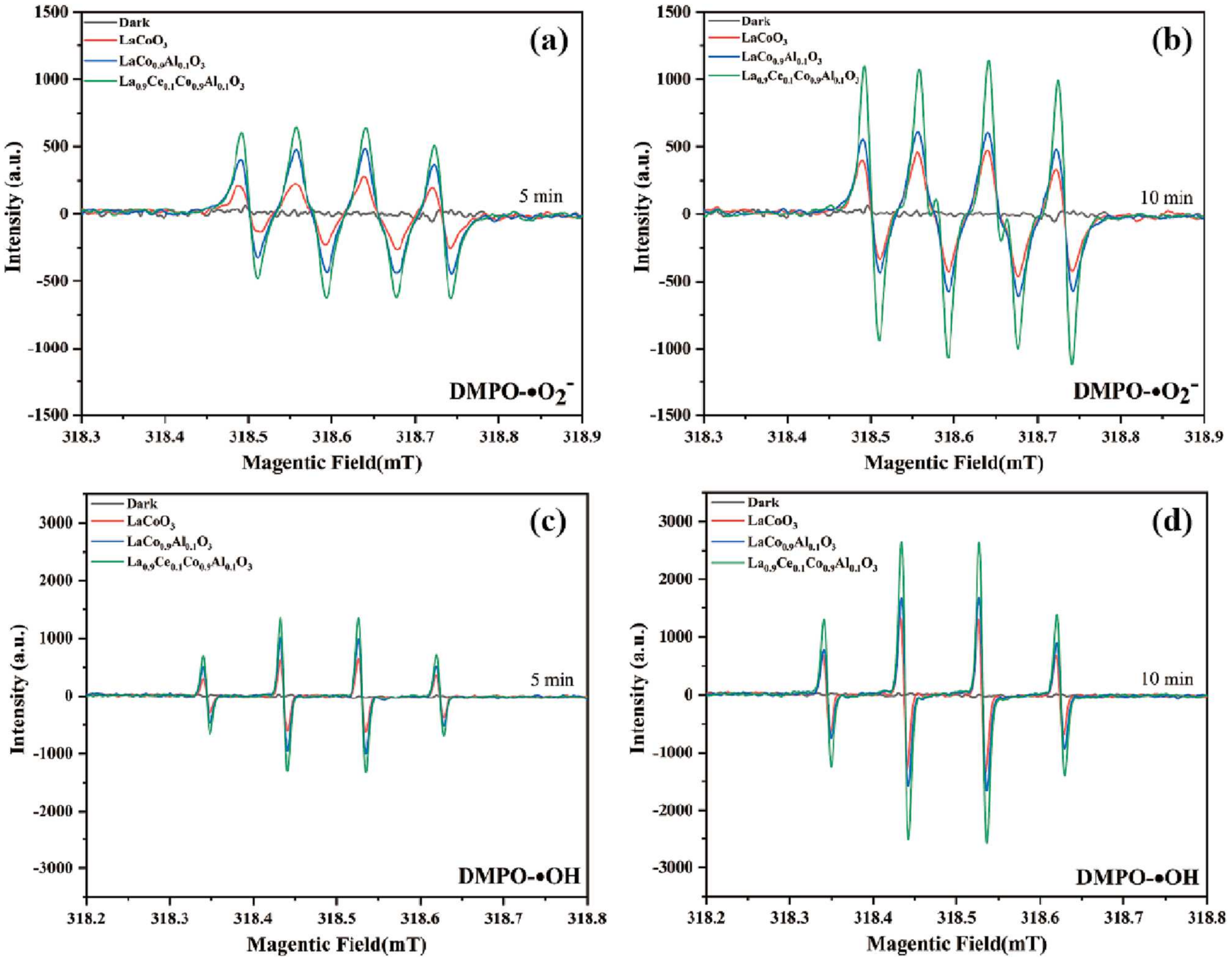

**Fig. 10.** EPR spectra of $LaCoO_3$, $LaCo_{0.9}Al_{0.1}O_3$ and $La_{0.9}Ce_{0.1}Co_{0.9}Al_{0.1}O_3$ nanoparticles after visible light irradiation: (a, b) $\bullet O_2^-$ and (c, d) •OH.

integrated areas of O2 to O1 increases upon the doping of Al and Ce, indicating that heteroatom doping at the A and B sites indeed facilitated the formation of oxygen vacancies. This was confirmed in EPR measurements (Fig. 8f), which clearly exhibited a spectral feature at $g = 2.001$ [56], and the intensity of the signal increased with the introduction of Al and Ce dopants. Note that the formation of oxygen vacancies is anticipated to promote the separation of photogenerated electron-hole pairs and enhance the photocatalytic activity, a critical step in the antibacterial activities [42], as observed below.

### 3.3. Antibacterial activities and mechanism

Gram-negative *E. coli* was selected as the illustrating example in the investigation of the antibacterial performances of the sample series. From Fig. 9a, it can be seen that in comparison to the blank control, the addition of the samples into the cultural media diminished markedly the bacterial growth both in the dark and under visible light irradiation. The antibacterial activity in the dark was likely due to the trace of dissolved ions that were bound to bacterial cells and membrane proteins, thus preventing the gene expression of enzymes and functional proteins in the electron transport system [57]; and the performance was significantly enhanced under visible light irradiation. As shown in Fig. 9b, the antibacterial efficiencies of $LaCoO_3$, $LaCo_{0.9}Al_{0.1}O_3$ and $La_{0.9}Ce_{0.1}Co_{0.9}Al_{0.1}O_3$ under visible light irradiation for 30 min were 52%, 79.9% and 98.8%, respectively, in comparison to only 20.1%, 29.2% and 49.8% in the dark. The fact that $La_{0.9}Ce_{0.1}Co_{0.9}Al_{0.1}O_3$ exhibited the best antibacterial performance indicates the significant role of the doping of Al and Ce into $LaCoO_3$ in inhibiting bacterial growth, likely due to enhanced production of ROS that impede normal bacterial metabolism and damage cell membranes, in particular, when excited by visible light [58,59].

EPR measurements were then carried out to investigate the visible light-driven antibacterial mechanism of the samples. From Fig. 10 it can be seen that only a featureless profile was observed in the dark, suggesting no production of radical species by the various samples. Yet, under visible light photoirradiation, a quartet that corresponded to the DMPO-$\bullet O_2^-$ (intensity ratio 1:1:1:1, Fig. 10 a-b) and DMPO-•OH (intensity ratio 1:2:2:1, Fig. 10c-d) adducts can be readily resolved, and the intensity increased with prolonged exposure. Furthermore, one can see that the DMPO-$\bullet O_2^-$ and DMPO-•OH signals became intensified from $LaCoO_3$ (red curve) to $LaCo_{0.9}Al_{0.1}O_3$ (blue curve) and further to $La_{0.9}Ce_{0.1}Co_{0.9}Al_{0.1}O_3$ (green curve), confirming the significant role of Al and Ce doping in ROS production (Fig. 10a-d). This may be attributed to the formation of structural defects that improved the visible absorption and carrier separation efficiency of $LaCoO_3$ [50]. In addition, the Ce and Al co-doped $LaCoO_3$ exhibited good stability (Figure S5), which facilitated a long-lasting antibacterial activity under visible light irradiation [34,60].

The above results show that codoping of the A and B sites in $LaCoO_3$ ($La_{0.9}Ce_{0.1}Co_{0.9}Al_{0.1}O_3$) led to markedly enhanced antibacterial performance under visible light irradiation. This can be ascribed to the following factors. (a) Ce and Al codoping facilitates the formation of oxygen vacancies in $LaCoO_{3,}$ which enhances ROS production and adsorption of bacteria [42]. (b) Ce and Al ions occupy the $LaCoO_3$

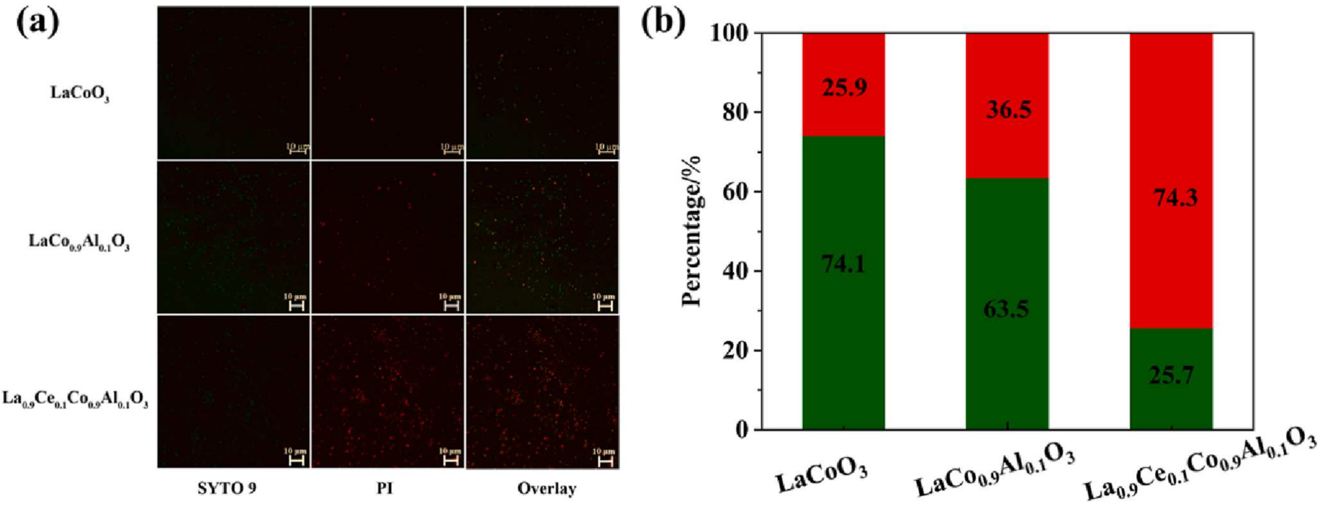

**Fig. 11.** (a) Stained images of live/dead bacteria after the treatment of different nanomaterials and (b) the related quantitative analysis results.

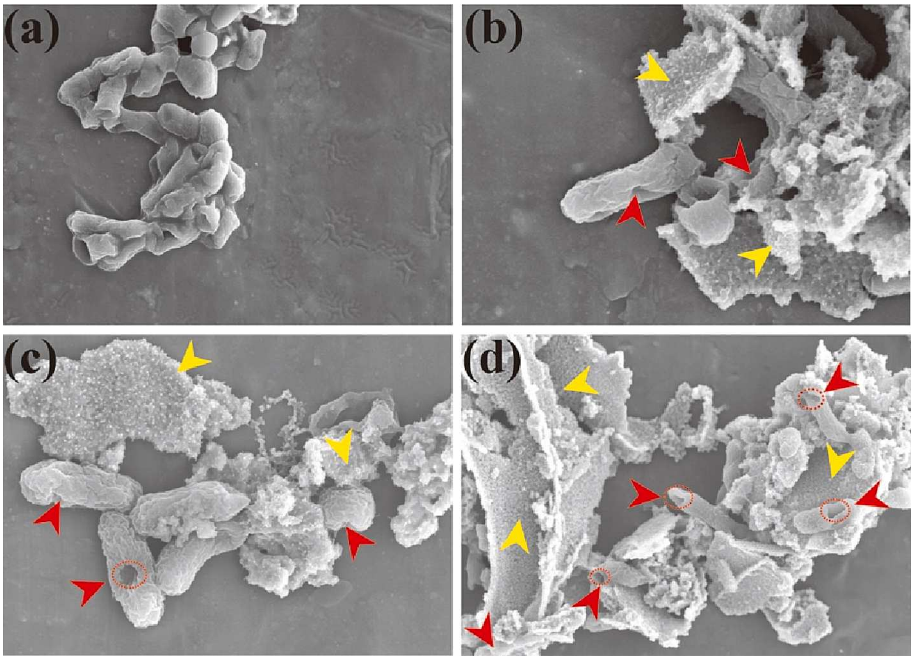

**Fig. 12.** SEM images of *E. coli* (a) treated without nanomaterials, (b) treated with $LaCoO_3$ nanomaterials, (c) treated with $LaCo_{0.9}Al_{0.1}O_3$ nanomaterials, (d) treated with $La_{0.9}Ce_{0.1}Co_{0.9}Al_{0.1}O_3$ nanomaterials.

lattices, enhance electron traps and active centers and accelerate the photocatalytic reaction process [26,44]. (c) Additional contributions of $La_{0.9}Ce_{0.1}Co_{0.9}Al_{0.1}O_3$ may arise from ion solubilization effect (Table S4) [61,62]. Photographs and statistical analysis of *E. coli* after the treatment of $La_{0.9}Ce_{0.1}Co_{0.9}Al_{0.1}O_3$ at different concentrations are shown in Figure S6 and S7. The antibacterial effect of $La_{0.9}Ce_{0.1}Co_{0.9}Al_{0.1}O_3$ under visible light increased with the increase of the sample concentration, and reached ca. 100% at 1 mg/mL.

To further investigate the antibacterial mechanism, the treated bacteria were stained with membrane permeable dye SYTO 9 and non-membrane permeable dye PI. SYTO 9 can be used to mark both live and dead cells, whereas PI can only mark cells with damaged cell membranes [62]. The live/dead staining assay in Fig. 11a showed that the $La_{0.9}Ce_{0.1}Co_{0.9}Al_{0.1}O_3$ exhibited the best antibacterial activity, with the largest fraction of dead cells (red fluorescence) at 74.3%, as compared to only 25.9% and 36.5% with $LaCoO_3$ and $LaCo_{0.9}Al_{0.1}O_3$, respectively (Fig. 11b). Because the bacterial membrane is a critical protective barrier for the cells, it can be inferred that light-driven ROS production induces lipid peroxidation in the cell membrane, which enhances cell membrane permeability and ultimately leads to intracellular protein leak and irreversible damage to bacteria [63].

This is indeed confirmed in SEM measurements (Fig. 12). In comparison to the pristine *E. coli* cells which exhibited a smooth surface (Fig. 12a), photodynamic treatment by $La_{0.9}Ce_{0.1}Co_{0.9}Al_{0.1}O_3$ led to the formation of a large number of folds and breakages of the bacterial cell membranes (red arrows, Fig. 12d), as compared to those with $LaCoO_3$ (Fig. 12b) and $LaCo_{0.9}Al_{0.1}O_3$ (Fig. 12c). Importantly, some nanoparticles remained attached to the bacterial surface (yellow arrows, Fig. 12) even after washing. Such intimate contacts most likely facilitated the rapid and concentrated transfer of the generated ROS (e.g., $\bullet O_2^-$ and •OH) to the bacterial cells during the photodynamic treatment. The morphological changes in the bacteria provide further evidence that the produced ROS damaged the *E. coli* cells, which allowed for the release of intercellular components, such as proteins and DNA [63,64].

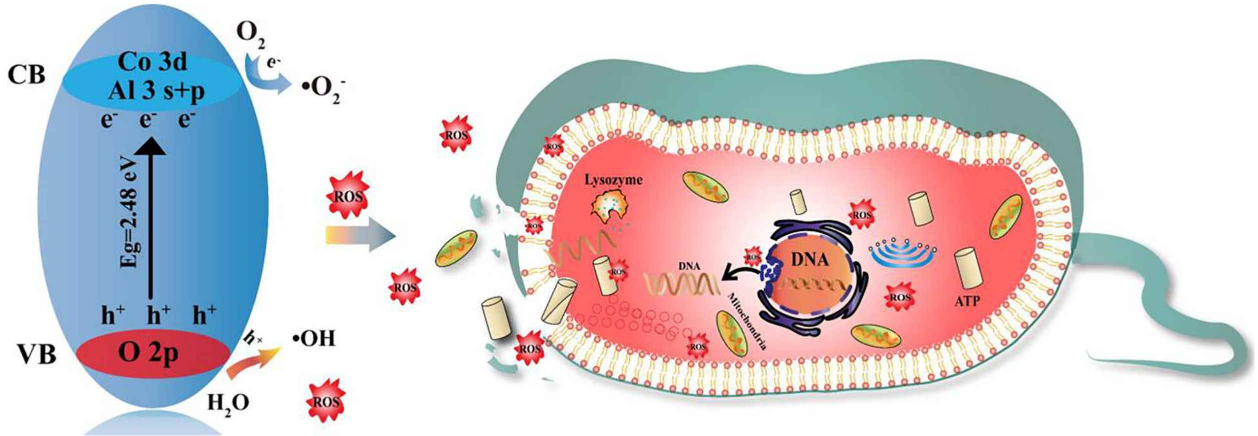

**Fig. 13.** Schematic diagram of the antibacterial mechanism of $La_{0.9}Ce_{0.1}Co_{0.9}Al_{0.1}O_3$ with doping-induced oxygen vacancies.

Based on the experimental and DFT results, a schematic diagram of the antibacterial mechanism of $La_{0.9}Ce_{0.1}Co_{0.9}Al_{0.1}O_3$ under visible light irradiation is depicted in Fig. 13, to illustrate the key role of oxygen vacancies in the antibacterial action. The antibacterial mechanism is proposed as follows: (a) $La_{0.9}Ce_{0.1}Co_{0.9}Al_{0.1}O_3$ acts as an electron donor. Upon irradiation by visible light, electrons in the valence band consisting of the O 2p orbitals leap to the conduction band consisting of the Co 3d and Al 3 s + p orbitals through the defective energy level formed by oxygen vacancies, and $H_2O$ is oxidized by the holes in the valence band to generate hydroxyl radicals ($\bullet$OH). (b) Oxygen vacancies acts as catalytical active centers and as electron traps and oxygen adsorption centers for the facile reduction of $O_2$ to superoxide anions ($\bullet O_2^-$). At the same time, the redox chemistry of $Ce^{4+}/Ce^{3+}$ enables the efficient transfer of electrons, thus greatly enhancing the catalytic performance. (c) ROS is the main antibacterial reagents, where the generated superoxide anion and hydroxyl radicals attack the surface of the bacterial cells damaging the cell membranes. Additional (minor) contributions may arise from the trace amounts of dispersed ions from the samples.

## 4. Conclusions

In this study, the deliberate integration of theory and experiment led to the development of effective photocatalysts that exhibited remarkable photodynamic antibacterial activity under visible light irradiation. Results from DFT calculations showed the significant impacts of Ce and Al doping at the A and B sites on the formation of oxygen vacancies in $LaCoO_3$, which facilitated the adsorption of oxygen and water molecules, a critical step in the photocatalytic production of ROS. This was indeed confirmed in experimental measurements, where $La_{0.9}Ce_{0.1}Co_{0.9}Al_{0.1}O_3$ was synthesized by a facile sol–gel method, and exhibited a significantly enhanced antibacterial efficiency of 98.8% after visible irradiation for 30 min, as compared to 46.8% for undoped $LaCoO_3$. This was accounted for by the formation of oxygen vacancies, which effectively narrowed the materials band gap, extended the optical absorption from the UV to the visible range, and enhanced the carrier separation and transport efficiency. This ultimately led to the enhanced production of ROS and hence inhibition of bacterial growth. In conclusion, results from this work offer a unique strategy based on defect engineering for the rational design of high-performance perovskite photocatalysts. Such fundamental insights may be exploited for the further improvement of the visible-light antimicrobial activity as well as photovoltaic performance, among others.

## Declaration of Competing Interest

The authors declare that they have no known competing financial interests or personal relationships that could have appeared to influence the work reported in this paper.

## Data availability

Data will be made available on request.

## Acknowledgments

This work was supported by National Natural Science Foundation of China for Young Scholar (51802185), and Foundation of Key Laboratory of Clay Mineral Applied Research of Gansu Province, Lanzhou Institute of Chemical Physics, Chinese Academy of Sciences (CMAR-2022-03). S. W. C. thanks the National Science Foundation (CBET-1848841) for partial support of the work.

## Appendix A. Supplementary data

Supplementary data to this article can be found online at https://doi.org/10.1016/j.cej.2023.142710.

## References

[1] P.W. Taylor, P.D. Stapleton, J. Paul Luzio, New ways to treat bacterial infections, Drug Discovery Today 7 (2002) 1086–1091.

[2] C.R. Paula, V.L. Krebs, M.E. Auler, L.S. Ruiz, F.E. Matsumoto, E.H. Silva, E.M. Diniz, F.A. Vaz, Nosocomial infection in newborns by *Pichia anomala* in a Brazilian intensive care unit, Medical Mycology August, 44 (2006) 479-484.

[3] S. Arancia, S. Sandini, A. Cassone, F. De Bernardis, Use of 65kDa mannoprotein gene primers in PCR methods for the identification of five medically important *Candida* species, Mol. Cellular Probes 23 (2009) 218–226.

[4] J.P. Ruparelia, A.K. Chatterjee, S.P. Duttagupta, S. Mukherji, Strain specificity in antimicrobial activity of silver and copper nanoparticles, Acta Biomaterialia 4 (2008) 707–716.

[5] M.I. Din, R. Rehan, Synthesis, Characterization, and Applications of Copper Nanoparticles, Anal. Letters 50 (2016) 50–62.

[6] R. Yoksan, S. Chirachanchai, Silver nanoparticles dispersing in chitosan solution: Preparation by γ-ray irradiation and their antimicrobial activities, Mater. Chem. Phys. 115 (2009) 296–302.

[7] Y. Li, P. Leung, L. Yao, Q.W. Song, E. Newton, Antimicrobial effect of surgical masks coated with nanoparticles, J. Hosp. Infect. 62 (2006) 58–63.

[8] F. Martinez-Gutierrez, P.L. Olive, A. Banuelos, E. Orrantia, N. Nino, E.M. Sanchez, F. Ruiz, H. Bach, Y. Av-Gay, Synthesis, characterization, and evaluation of antimicrobial and cytotoxic effect of silver and titanium nanoparticles, Nanomedicine 6 (2010) 681–688.

[9] S.K. Das, A.R. Das, A.K. Guha, Gold nanoparticles: microbial synthesis and application in water hygiene management, Langmuir 25 (2009) 8192–8199.

[10] A. Wang, P. Zhou, D. Tian, H. Zhang, Z. Xiong, Y. Du, C. He, Y. Yuan, T. Chen, Y. Liu, B. Lai, Enhanced oxidation of fluoroquinolones by visible light-induced peroxydisulfate: The significance of excited triplet state species, Appl. Catal. B: Environ. 316 (2022), 121631.

[11] D. Zu, H. Wang, S. Lin, G. Ou, H. Wei, S. Sun, H. Wu, Oxygen-deficient metal oxides: Synthesis routes and applications in energy and environment, Nano Res. 12 (2019) 2150–2163.

[12] X. Sun, X. Zhang, Y. Xie, Surface Defects in Two-Dimensional Photocatalysts for Efficient Organic Synthesis, Matter 2 (2020) 842–861.

[13] S.A. Adonin, L.I. Udalova, P.A. Abramov, A.S. Novikov, I.V. Yushina, I.V. Korolkov, E.Y. Semitut, T.A. Derzhavskaya, K.J. Stevenson, P.A. Troshin, M.N. Sokolov, V. P. Fedin, A Novel Family of Polyiodo-Bromoantimonate(III) Complexes: Cation-Driven Self-Assembly of Photoconductive Metal-Polyhalide Frameworks, Chemistry 24 (2018) 14707–14711.

[14] S.A. Adonin, I.D. Gorokh, A.S. Novikov, D.G. Samsonenko, I.V. Yushina, M. N. Sokolov, V.P. Fedin, Halobismuthates with halopyridinium cations: appearance or non-appearance of unusual colouring, CrystEngComm 20 (2018) 7766–7772.

[15] S.A. Adonin, A.N. Usoltsev, A.S. Novikov, B.A. Kolesov, V.P. Fedin, M.N. Sokolov, One- and Two-Dimensional Iodine-Rich Iodobismuthate(III) Complexes: Structure, Optical Properties, and Features of Halogen Bonding in the Solid State, Inorg. Chem. 59 (2020) 3290–3296.

[16] Y. Wang, X. Wang, M. Antonietti, Polymeric graphitic carbon nitride as a heterogeneous organocatalyst: from photochemistry to multipurpose catalysis to sustainable chemistry, Angew. Chem. Int. Ed. 51 (2012) 68–89.

[17] J. Hwang, R.R. Rao, L. Giordano, Y. Katayama, Y. Yu, Y. Shao-Horn, Perovskites in catalysis and electrocatalysis, Science 358 (2017) 751–756.

[18] F. Nichols, K.I. Ozoemena, S. Chen, Electrocatalytic generation of reactive species and implications in microbial inactivation, Chin. J. Catal. 43 (2022) 1399–1416.

[19] D. Tian, H. Zhou, H. Zhang, P. Zhou, J. You, G. Yao, Z. Pan, Y. Liu, B. Lai, Heterogeneous photocatalyst-driven persulfate activation process under visible light irradiation: From basic catalyst design principles to novel enhancement strategies, Chem. Eng. J. 428 (2022), 131166.

[20] C. Singh, A. Wagle, M. Rakesh, Doped $LaCoO_3$ perovskite with Fe: A catalyst with potential antibacterial activity, Vacuum 146 (2017) 468–473.

[21] S. Tasleem, M. Tahir, Constructing $La_xCo_yO_3$ Perovskite Anchored 3D g-$C_3N_4$ Hollow Tube Heterojunction with Proficient Interface Charge Separation for Stimulating Photocatalytic $H_2$ Production, Energy Fuels 35 (2021) 9727–9746.

[22] Y. Tong, J. Wu, P. Chen, H. Liu, W. Chu, C. Wu, Y. Xie, Vibronic Superexchange in Double Perovskite Electrocatalyst for Efficient Electrocatalytic Oxygen Evolution, J. Am. Chem. Soc. 140 (2018) 11165–11169.

[23] J. Yang, S. Hu, Y. Fang, S. Hoang, L. Li, W. Yang, Z. Liang, J. Wu, J. Hu, W. Xiao, C. Pan, Z. Luo, J. Ding, L. Zhang, Y. Guo, Oxygen Vacancy Promoted $O_2$ Activation over Perovskite Oxide for Low-Temperature CO Oxidation, ACS Catal. 9 (2019) 9751–9763.

[24] J. Chen, H. Arandiyan, X. Gao, J. Li, Recent Advances in Catalysts for Methane Combustion, Catal. Surv. Asia 19 (2015) 140–171.

[25] L. Wang, T. Ma, S. Dai, T. Ren, Z. Chang, L. Dou, M. Fu, X. Li, Experimental study on the high performance of Zr doped $LaCoO_3$ for solar thermochemical CO production, Chem. Eng. J. 389 (2020), 124426.

[26] A.A. Ansari, S.F. Adil, M. Alam, N. Ahmad, M.E. Assal, J.P. Labis, A. Alwarthan, Catalytic performance of the Ce-doped $LaCoO_3$ perovskite nanoparticles, Sci. Rep. 10 (2020) 15012.

[27] M. Wang, T. Zhao, X. Dong, M. Li, H. Wang, Effects of Ce substitution at the A-site of $LaNi_{0.5}Fe_{0.5}O_3$ perovskite on the enhanced catalytic activity for dry reforming of methane, Appl. Catal. B: Environ. 224 (2018) 214–221.

[28] L. Tang, Z. Zhao, K. Li, X. Yu, Y. Wei, J. Liu, Y. Peng, Y. Li, Y. Chen, Highly Active Monolith Catalysts of $LaKCoO_3$ Perovskite-type Complex Oxide on Alumina-washcoated Diesel Particulate Filter and the Catalytic Performances for the Combustion of Soot, Catal. Today 339 (2020) 159–173.

[29] S. Lu, G. Wang, S. Chen, H. Yu, F. Ye, X. Quan, Heterogeneous activation of peroxymonosulfate by $LaCo_{1-x}Cu_xO_3$ perovskites for degradation of organic pollutants, J. Hazard. Mater. 353 (2018) 401–409.

[30] Y. Ham, T. Hisatomi, Y. Goto, Y. Moriya, Y. Sakata, A. Yamakata, J. Kubota, K. Domen, Flux-mediated doping of $SrTiO_3$ photocatalysts for efficient overall water splitting, J. Mater. Chem. A 4 (2016) 3027–3033.

[31] Y. Goto, T. Hisatomi, Q. Wang, T. Higashi, K. Ishikiriyama, T. Maeda, Y. Sakata, S. Okunaka, H. Tokudome, M. Katayama, S. Akiyama, H. Nishiyama, Y. Inoue, T. Takewaki, T. Setoyama, T. Minegishi, T. Takata, T. Yamada, K. Domen, A Particulate Photocatalyst Water-Splitting Panel for Large-Scale Solar Hydrogen Generation, Joule 2 (2018) 509–520.

[32] T. Takata, K. Domen, Defect engineering of photocatalysts by doping of aliovalent metal cations for efficient water splitting, J. Phys. Chem. C 113 (2009) 19386–19388.

[33] A. Yamakata, H. Yeilin, M. Kawaguchi, T. Hisatomi, J. Kubota, Y. Sakata, K. Domen, Morphology-sensitive trapping states of photogenerated charge carriers on $SrTiO_3$ particles studied by time-resolved visible to Mid-IR absorption spectroscopy: The effects of molten salt flux treatments, J. Photochem. Photobiol. A: Chem. 313 (2015) 168–175.

[34] Z. Jin, R. Hu, H. Wang, J. Hu, T. Ren, One-step impregnation method to prepare direct *Z*-scheme $LaCoO_3$/g-$C_3N_4$ heterojunction photocatalysts for phenol degradation under visible light, Appl. Surf. Sci. 491 (2019) 432–442.

[35] G. Kresse, J. Furthmüller, Efficient iterative schemes for ab initio total-energy calculations using a plane-wave basis set, Phys. Rev. B 54 (1996) 11169.

[36] G. Kresse, D. Joubert, From ultrasoft pseudopotentials to the projector augmented-wave method, Phys. Rev. B 59 (1999) 1758.

[37] S. Grimme, J. Antony, S. Ehrlich, H. Krieg, A consistent and accurate ab initio parametrization of density functional dispersion correction (DFT-D) for the 94 elements H-Pu, J. Chem. Phys. 132 (2010), 154104.

[38] G. Henkelman, B.P. Uberuaga, H. Jónsson, A climbing image nudged elastic band method for finding saddle points and minimum energy paths, J. Chem. Phys. 113 (2000) 9901–9904.

[39] Y. Liu, X. Kong, X. Guo, Q. Li, J. Ke, R. Wang, Q. Li, Z. Geng, J. Zeng, Enhanced $N_2$ Electroreduction over $LaCoO_3$ by Introducing Oxygen Vacancies, ACS Catal. 10 (2019) 1077–1085.

[40] Z. Cui, C. Xiao, Y. Lv, Q. Li, R. Sa, Z. Ma, Adsorption behavior of CO, $CO_2$, $H_2$, $H_2O$, NO, and $O_2$ on pristine and defective 2D monolayer ferromagnetic $Fe_3GeTe_2$, Appl. Surf. Sci. 527 (2020), 146894.

[41] H. Li, J. Li, Z. Ai, F. Jia, L. Zhang, Oxygen Vacancy-Mediated Photocatalysis of BiOCl: Reactivity, Selectivity, and Perspectives, Angew. Chem. Int. Ed. 57 (2018) 122–138.

[42] Y. Zhou, Y. Guo, J. Li, W. Wei, D. Li, L. Luo, X. Xu, Z. Zhou, Excellent antibacterial activities in the dark of ZnO nanoflakes with oxygen vacancies on exposed 2110 facets, J. Mater. Chem. A 8 (2020) 11511–11514.

[43] Z. Gu, Z. Cui, Z. Wang, T. Chen, P. Sun, D. Wen, Reductant-free synthesis of oxygen vacancies-mediated $TiO_2$ nanocrystals with enhanced photocatalytic NO removal performance: An experimental and DFT study, Appl. Surf. Sci. 544 (2021), 148923.

[44] J. Zhu, Y. Zhao, D. Tang, Z. Zhao, S.A.C. Carabineiro, Aerobic selective oxidation of alcohols using $La_{1-x}Ce_xCoO_3$ perovskite catalysts, J. Catal. 340 (2016) 41–48.

[45] T. Suwannaruang, P. Kidkhunthod, T. Butburee, H.P. Shivaraju, B. Shahmoradi, K. Wantala, Facile synthesis of cooperative mesoporous-assembled $Ce_xSr_{1-x}Fe_xTi_{1-x}O_3$ perovskite catalysts for enhancement beta-lactam antibiotic photodegradation under visible light irradiation, Surf. Interfaces 23 (2021), 101013.

[46] V. Aswin, P. Kumar, P. Singh, A. Gupta, S. Rayaprol, A. Dogra, Influence of Al doping in $LaCoO_3$ on structural, electrical and magnetic properties, J. Mater. Sci. 50 (2014) 366–373.

[47] H.A. Pérez, C.A. López, L.E. Cadús, F.N. Agüero, Catalytic feasibility of Ce-doped $LaCoO_3$ systems for chlorobenzene oxidation: An analysis of synthesis method, J. Rare Earths 40 (2022) 897–905.

[48] A.A. Ansari, N. Ahmad, M. Alam, S.F. Adil, S.M. Ramay, A. Albadri, A. Ahmad, A. M. Al-Enizi, B.F. Alrayes, M.E. Assal, A.A. Alwarthan, Physico-chemical properties and catalytic activity of the sol-gel prepared Ce-ion doped $LaMnO_3$ perovskites, Sci. Rep. 9 (2019) 7747.

[49] C.R. Manjunatha, B.M. Nagabhushana, M.S. Raghu, S. Pratibha, N. Dhananjaya, A. Narayana, Perovskite lanthanum aluminate nanoparticles applications in antimicrobial activity, adsorptive removal of Direct Blue 53 dye and fluoride, Mater. Sci. Eng. C 101 (2019) 674–685.

[50] G. Fan, Z. Chen, Z. Yan, B. Du, H. Pang, D. Tang, J. Luo, J. Lin, Efficient integration of plasmonic Ag/AgCl with perovskite-type $LaFeO_3$: Enhanced visible-light photocatalytic activity for removal of harmful algae, J. Hazard. Mater. 409 (2021), 125018.

[51] M. Mousavi, A. Habibi-Yangjeh, M. Abitorabi, Fabrication of novel magnetically separable nanocomposites using graphitic carbon nitride, silver phosphate and silver chloride and their applications in photocatalytic removal of different pollutants using visible-light irradiation, J. Colloid Interface Sci. 480 (2016) 218–231.

[52] M.M. Natile, G. Eger, P. Batocchi, F. Mauvy, A. Glisenti, Strontium and copper doped $LaCoO_3$: New cathode materials for solid oxide fuel cells? Int. J. Hydrogen Energy 42 (2017) 1724–1735.

[53] L. Rosenberger, R. Baird, E. McCullen, G. Auner, G. Shreve, XPS analysis of aluminum nitride films deposited by plasma source molecular beam epitaxy, Surf. Interface Anal. 40 (2008) 1254–1261.

[54] P. Garcia-Muñoz, F. Fresno, C. Lefevre, D. Robert, N. Keller, Synergy effect between photocatalysis and heterogeneous photo-Fenton catalysis on Ti-doped $LaFeO_3$ perovskite for high efficiency light-assisted water treatment, Catal, Sci. Technol. 10 (2020) 1299–1310.

[55] J. Qian, T. Wang, Z. Zhang, Y. Liu, J. Li, D. Gao, Engineered spin state in Ce doped $LaCoO_3$ with enhanced electrocatalytic activity for rechargeable Zn-Air batteries, Nano Energy 74 (2020), 104948.

[56] Q. Gao, J. Meng, Y. Yang, Q. Lin, Y. Lu, X. Wei, J. Li, G. Han, Z. Zhang, Zirconium doping in calcium titanate perovskite oxides with surface nanostep structure for promoting photocatalytic hydrogen evolution, Appl. Surf. Sci. 542 (2021), 148544.

[57] M.D. Rojas-Andrade, G. Chata, D. Rouholiman, J. Liu, C. Saltikov, S. Chen, Antibacterial mechanisms of graphene-based composite nanomaterials, Nanoscale 9 (2017) 994–1006.

[58] R.K. Upadhyay, N. Soin, S.S. Roy, Role of graphene/metal oxide composites as photocatalysts, adsorbents and disinfectants in water treatment: a review, RSC Adv. 4 (2014) 3823–3851.

[59] X. Gao, M. Li, F. Zhou, X. Wang, S. Chen, J. Yu, Flexible zirconium doped strontium titanate nanofibrous membranes with enhanced visible-light photocatalytic performance and antibacterial activities, J. Colloid Interface Sci. 600 (2021) 127–137.

[60] Y. Gu, G. Teng, X. Jin, L. Wang, Z. Qiang, W. Ma, C. Zhang, Shape-Controlled Synthesis of Coral-like ZnO/C-$ZnFe_2O_4$ Hierarchical Structures and Their Improved Photocatalytic Antibacterial Efficiency under Visible Light Illumination, Ind. Eng. Chem. Res. 59 (2020) 11219–11231.

[61] L. Zhang, P.Y. Tan, C.L. Chow, C.K. Lim, O.K. Tan, M.S. Tse, C.C. Sze, Antibacterial activities of mechanochemically synthesized perovskite strontium titanate ferrite metal oxide, Colloids Surf. A: Physicochem. Eng. Asp. 456 (2014) 169–175.

[62] Y. Chu, X. Tan, Z. Shen, P. Liu, N. Han, J. Kang, X. Duan, S. Wang, L. Liu, S. Liu, Efficient removal of organic and bacterial pollutants by Ag-$La_{0.8}Ca_{0.2}Fe_{0.94}O_{3-\delta}$ perovskite via catalytic peroxymonosulfate activation, J. Hazard. Mater. 356 (2018) 53–60.

[63] X. Zhao, K. Drlica, Reactive oxygen species and the bacterial response to lethal stress, Curr. Opin. Microbiol. 21 (2014) 1–6.

[64] R.M. Burger, K. Drlica, Superoxide protects *Escherichia coli* from bleomycin mediated lethality, J. Inorg. Biochem. 103 (2009) 1273–1277.